Journal of Alloys and Compounds 909 (2022) 164800

Contents lists available at ScienceDirect

Journal of Alloys and Compounds

journal homepage: www.elsevier.com/locate/jalcom

Location-dependent deformation behavior of additively manufactured copper and copper-carbon nanotube composite

Maryam Sadeghilaridjani, Leila Ladani*

School for Engineering of Matter, Transport and Energy, Arizona State University, Tempe, AZ 85287, USA

ARTICLE INFO

Article history:
Received 6 February 2022
Received in revised form 25 March 2022
Accepted 26 March 2022
Available online 31 March 2022

Keywords:
Laser powder bed fusion additive manufacturing
Copper
Carbon nanotube
Creep
Strain Rate Sensitivity

ABSTRACT

Pure copper (Cu) and copper-carbon nanotube (Cu-CNTs) alloys were fabricated using laser powder bed fusion additive manufacturing (LPBF-AM) with a relatively high density. Their location-dependent (i.e., distance from build plate) microstructure and nanomechanical properties at room temperature were investigated. The microstructure of the as-build Cu showed ~40% lower porosity as compared to the AM Cu-CNTs. The amount of porosity was dependent on location for Cu sample with the bottom surface had ~61% lower porosity as compared to the top surface, however the change in porosity was negligible for as-build Cu-CNTs depending on the distance from the build plate. With the addition of 0.5 wt% CNTs, the mechanical properties of the composite were decreased slightly may be due to porosity, weak interfacial bonding of Cu and CNTs, CNT agglomeration, and degraded CNTs. Nanoindentation tests showed that the average modulus value and hardness of the composites were in the range of 40–80 GPa and 0.7–1.1 GPa, respectively depending on the strain rates and distance from the build plate; 18% and 25% decreases were achieved compared with pure copper, respectively. Creep displacement also increased for as-build Cu-CNTs as compared to the pure Cu. Further, for each system, increase in porosity led to increase in strain rate sensitivity and decrease in maximum creep displacement.

1. Introduction

Due to its excellent thermal and electrical conductivity [1–3], copper (Cu) and its alloys have attracted great attention. They are used as electrical conductors in applications ranging from automotive to semiconductor and chip manufacturing. Cu is also used for thermal management in numerous applications. Additionally, in applications such as lightings shields used in aerospace applications, the weight becomes an important factor. Therefore, lighter materials with high thermal and electrical conductivity are required for automobiles and aircrafts to enhance fuel efficiencies and reduce carbon footprint [4].

Additionally, copper suffers from two major issues at nanoscale. The first issue is the increased resistivity. This effect is shown in Fig. 1(b). As seen in this figure the copper resistance as the dimensions decrease, increases relatively faster than CNTs.

The second issue with use of copper in smaller scale is the issue of electro-migration [3,4]. Electro-migration (EM) is the transport of material caused by the gradual movement of the ions in a conductor due to momentum transfer between conducting electrons and diffusion metal atoms. This issue is exacerbated at nanoscale due to high current density in interconnects. The proposed solution is to use CNTs alongside with copper, a composite, to benefit from tunneling effect for electron transport and high ampacity of CNTs. It was shown previously that the CNT-copper composite has 100-fold ampacity of copper alone (Fig. 2) [5].

Recent research shows that nanostructured composites can produce and/or enhance multi-functionality in many different ways that traditional composite materials cannot [6]. Other efforts have embarked on producing highly functional interconnects such as [7], and optical interconnects [8]. However, their fabrication is still imperfect and none have been able to realize the full potential of CNTs.

Carbon nanotubes are very stable materials. Carbon has strong Sp2 hybrid bonds with its neighboring carbon atoms and no desire to bond to anything outside of the tube. Furthermore, the large curvature of the surface of the CNTs prevents adhesion of other materials. It was shown previously that CNTs have poor wettability to metals [9]. Metal surface tension plays an important role in this wetting behavior. Liquids with low surface tension such as water or other aquatic solutions can easily wet the CNTs, however, it was discovered by Ebbesen [10] that materials with surface tension higher than 100–200 mN/m generally do not wet the surface of

* Corresponding author.
E-mail address: ljannesa@asu.edu (L. Ladani).

https://doi.org/10.1016/j.jallcom.2022.164800
0925-8388/

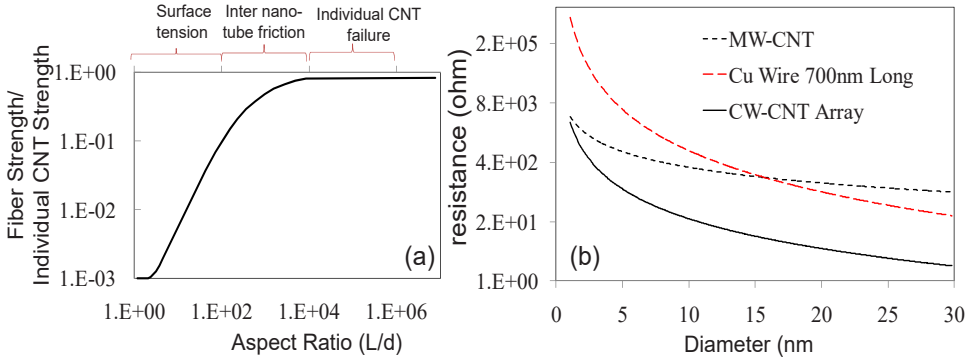

Fig. 1. (a) Tensile strength of a perfectly aligned bundle of CNTs as a function of aspect ratio [1] and (b) Theoretical resistance of vias filled with Cu and an array of single wall CNTs (SWCNTs) or one multiwall CNT (MWCNT) [2].

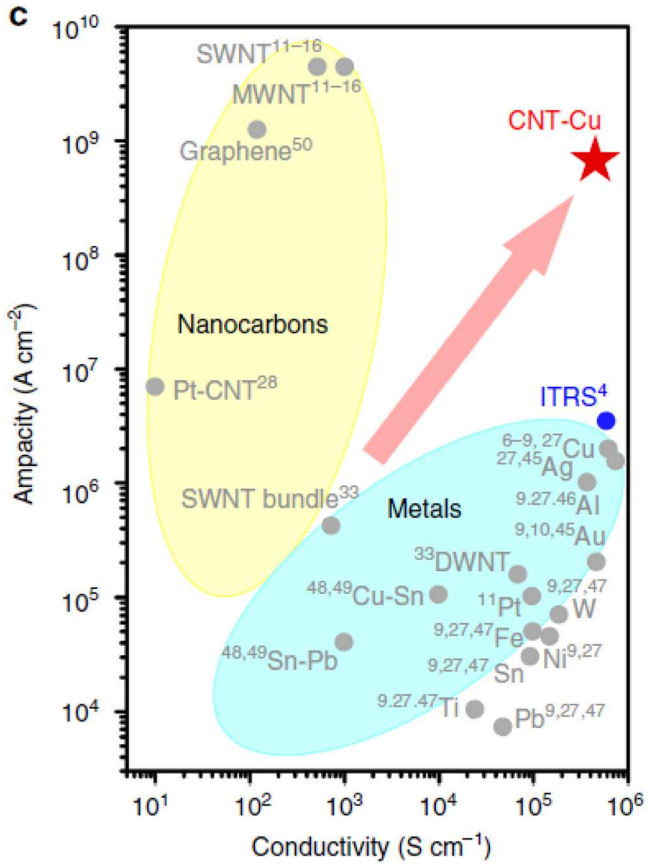

Fig. 2. Courtesy of Ashby plot of ampacity versus conductivity for various.

CNTs. Many have suggested chemically treating the CNT surfaces such as oxidation or acid treatments so that it could react with other materials. Using these approaches, researchers have used mostly electroless plating of CNTs [11–13]. However, these technologies are yet to achieve optimum results and full use of CNTs extraordinary properties [5–10].

Therefore, manufacturing is the main hinderance in replacing Cu with Cu-CNTs. Challenges such as difficulty to distribute CNTs homogeneously in the matrix need to be overcome [4]. Two major approaches to fabricate Cu-CNTs include: (i) powder-processing which involves making Cu-CNTs nanocomposite powders by mixing CNTs and Cu powders using mechanical alloying or ball milling, followed by compaction [4] and (ii) electrodeposition [4]. Complex structures are difficult to fabricate using these two techniques, hence there is a need for new and advanced fabrication techniques [3].

Additive manufacturing (AM) technique offers flexibility in design and allows the production of components with complex geometries by building the material using a bottom-up approach. At the same time AM can minimize waste and energy [2,11,12]. AM technology has been widely used to fabricate components made of steel, titanium, nickel, and aluminum alloys [13–30]. However, fabricating Cu using powder bed additive manufacturing poses several challenges. Cu is highly conductive and dissipates heat quickly. This means that much higher laser power is needed in order to sustain the melt pool and achieve a defect free build. Additionally, Cu is very reflective and does not absorb much of laser energy due to its low absorptivity at laser frequencies used in powder bed processes. This again, translates into need for higher laser powers. Fabrication of Cu alone has been attempted very scarcely by additive manufacturers and is still under heavy investigation [14,15]. However, challenging. there are several reports to fabricate Cu and its alloys using selective laser sintering (SLS) [31–33], selective laser melting (SLM) [34,35], and selective electron beam melting (SEBM) [2].

Addition of CNTs to Cu poses several other challenges and benefits.

However, fabrication of composite material such as Cu-CNT has not yet been achieved using AM powder bed processes. Adding nanotubes to the copper powder could pose challenges as it could potentially increase the explosibility index of the powder. However, addition of CNTs could potentially impact the absorption coefficient and improve heat absorption and allow sustainable melt pool. The manufacturing of these composites have bee discussed in another article. This article focuses on the local characterization of deformation mechanisms in the material.

2. Materials and methods

Spherical Cu powders (> 99.8% purity) with particles size in the range of 45–105 μm were obtained from the Stanford Advanced Materials (Lake Forest, CA, USA). The 0.5 wt% multi-walled carbon nanotube with purity of > 98%, outer diameter of 4–6 nm, and length of 10–20 μm (Nanostructured & Amorphous Materials, Inc., USA) were mixed with Cu powder using ball milling at room temperature for 2 h at speed of 300 rpm and ball to powder ratio of 5:1.

Given the small size of CNT, it is impractical to look at the distribution of CNTs using regular or scanning electron microscope. Therefore, elemental mapping is used to verify the uniform distribution of CNTs in Cu. EDS image of the Cu-CNT mix is provided in Fig. 3.

Concept Laser Mlab machine was used to fabricate the $10 \times 10 \times 10$ mm^3 Cu and Cu-CNTs cubes using laser powder bed fusion additive manufacturing. Laser powder bed additive manufacturing of the Cu and Cu-CNTs are conducted using a concept laser machine. Several parameters including laser power, laser speed and

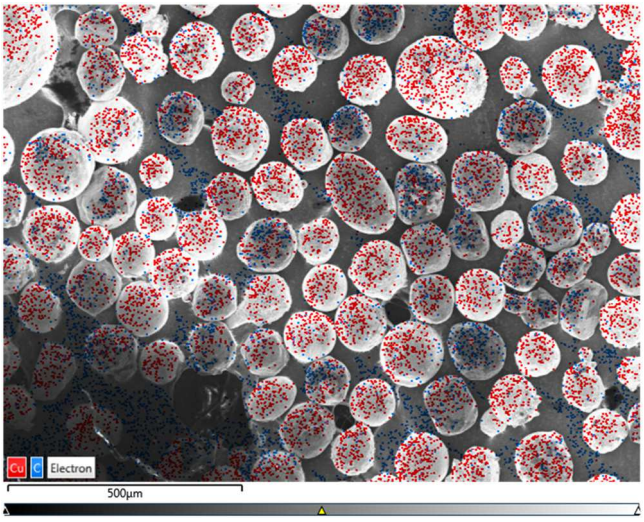

Fig. 3. Elemental mapping of Cu-CNT powder. The color-coded image shows relatively uniform distribution of CNTs in between Cu particles.

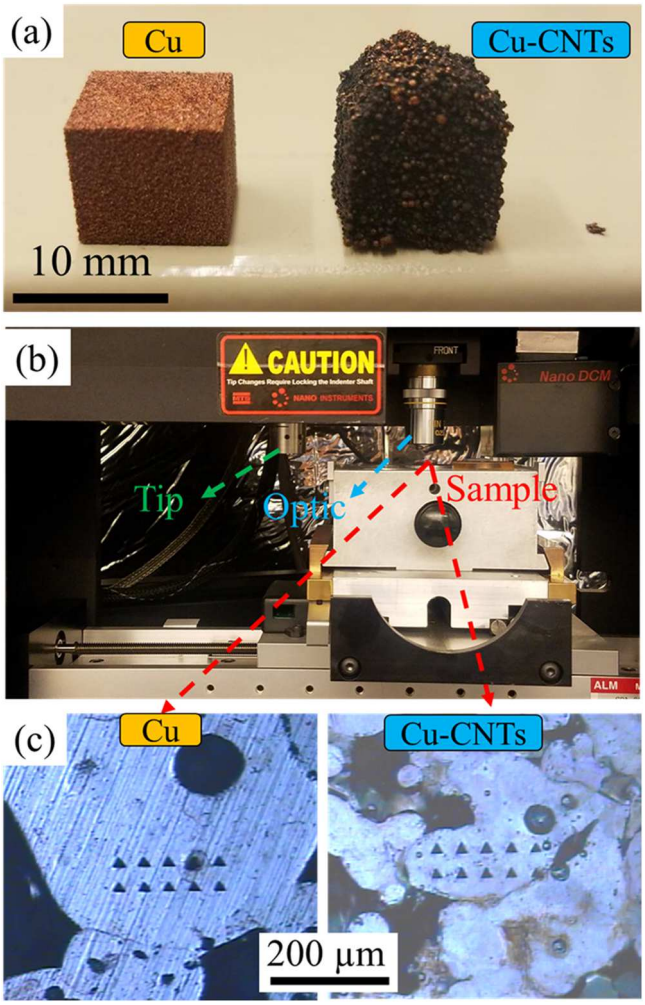

Fig. 4. (a) As-build Cu (left) and Cu-CNTs (right) cubes, (b) nanoindentation instrument used in current study, and (c) optical images of the indents on surface of Cu (left side) and Cu-CNTs (right side).

hatch spacing were varied systematically to identify parameters that result in higher density and less surface roughness. Those parameters for Cu were found to be hatch spacing of 90 µm, power of 93 W and speed of 47 mm/s and for Cu-CNT samples were found to achieved at hatch spacing of 100 µm, power of 93 W and speed of 47 mm/s [16]. Best samples were selected for local mechanical characterization. The as-build Cu and Cu-CNTs cubes are shown in Fig. 4(a). The samples were cut and polished to mirror surface finish for microstructural characterization using scanning electron microscope (SEM, Focused Ion Beam/SEM-Auriga-Zeiss, USA) equipped with energy dispersive spectroscopy (EDS). Nanoindentation was done using MTS Nano Indenter XP (KLA Corporation, Milpitas, California, USA) (Fig. 4(b)) with a diamond Berkovich tip at room temperature in displacement control mode and maximum displacement of 3000 nm. To study the strain rate sensitivity, strain rates were varied between 0.01/s, 0.05/s, and 0.25/s. Nanoindentation creep was evaluated at a displacement of 3000 nm using a constant strain rate of 0.05/s. The samples were held at the maximum displacement for 600 s followed by unloading. At least ten indents were performed under each test condition with 50 µm spacing between two indents to avoid overlap of their plastic zones. The optical images of the indents on both Cu and Cu-CNTs are shown in Fig. 4(c). For all tests, the thermal drift rate was kept below 0.05 nm/s.

3. Results and discussion

3.1. Microstructure characterization

The microstructure of all samples fabricated using laser powder bed fusion additive manufacturing under optimized processing conditions from top and bottom surfaces perpendicular to the build direction was analyzed through scanning electron microscopy. The goal was to investigate the location-dependent (i.e., distance from base plate) and composition-dependent changes in the structure and porosity. Fig. 5 and Fig. 6 summarize the microstructure characterization of samples. The SEM images of the top and bottom surfaces of the as-build Cu are presented in Fig. 5(a) and 2(b), respectively. The inset schematic shows the surface of interest. Some macropores were seen for the LPBF-AM samples due to lack of fusion and unmelted powder particles [35]. The ImageJ software was used to measure the area fraction of porosity for the samples. The results showed that the Cu sample fabricated using LPBF-AM had ~13% porosity on top surface and ~5% porosity on bottom surface. The lower porosity for bottom surface may be because of the re-melting of the previously solidified layers. In previous studies, the pure Cu parts fabricated using SLM and SLS showed the porous structure with the relative density of 82–88% and 76%, respectively [3,34,35]. In some studies, the high relative density of 98% was also reported which was obtained at high laser power sources [36] which was beyond the limitation of the AM machine used in this study. Fig. 5(c) and 2(d) show the SEM images of the as-build Cu-CNTs taken from the top and bottom surfaces, respectively. The calculated area fraction of porosity was ~15% for both surfaces of Cu-CNTs sample. Although, it has been reported that the addition of carbon enhances the powder's laser absorption rate and improve the relative density of parts [1,3], the as-build Cu-CNTs in the current study showed higher porosity. This may be due to fact that the laser energy absorbed by the CNT was not efficiently transferred to the Cu particles because of weak physical interaction and bonding between the Cu particles and CNTs. Elemental distribution for the as-build Cu-CNTs alloy from top and bottom surfaces was obtained using EDS analysis as shown in Fig. 6(a) and (b), respectively confirming the distribution of C in the material. CNTs seem to have agglomerated in the pores and surfaces.

3.2. Hardness, Young's Modulus, and Strain Rate Sensitivity (SRS)

The representative nanoindentation load-displacement plot randomly measured on the polished surface of the as-build Cu

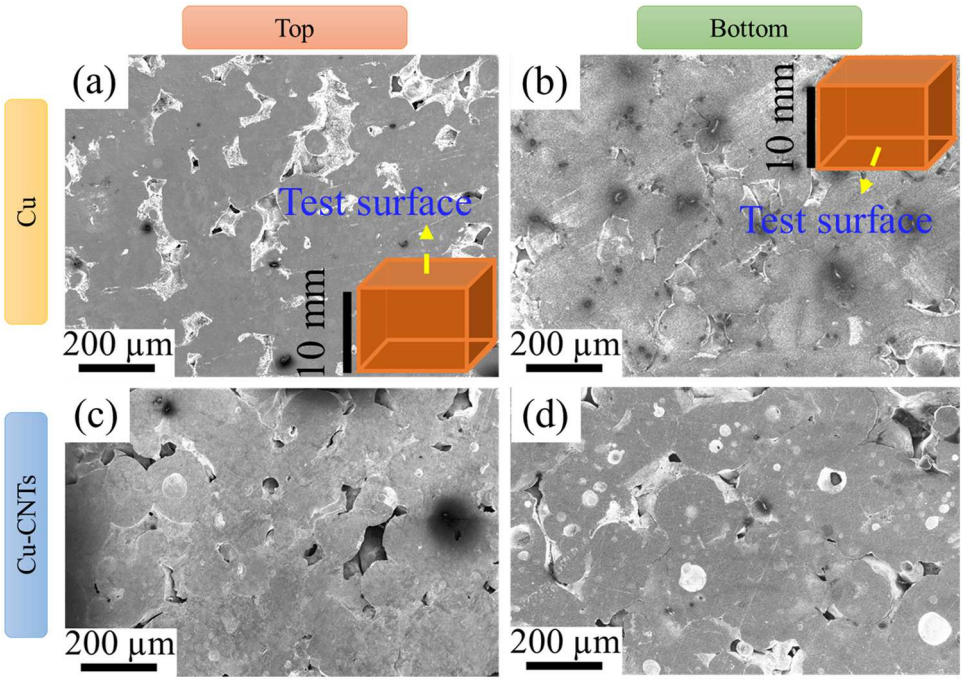

Fig. 5. Scanning electron microscopy (SEM) images of the laser powder bed fusion additively manufactured (LPBF-AM) Cu from (a) top surface and (b) bottom surface; SEM images of the as-build Cu-CNTs from (c) top surface and (b) bottom surface indicating higher amount of porosity for AM processed Cu-CNTs sample.

sample from top and bottom surfaces are shown in Fig. 7(a) and (b), respectively as a function of strain rate. The shift of load-displacement curves to higher load with increase in strain rate confirms the increase in hardness as strain rate increased, indication of positive strain rate sensitivity. This may be related to dislocations entanglement which had a pinning effect with straining at high strain rates [37]. The positive SRS was observed for several other alloys including Cu, Ni, Cr, bulk metallic glasses, and high entropy alloys [38–41]. The corresponding hardness as a function of displacement at three different strain rates for top and bottom surfaces of AM fabricated Cu are presented in Fig. 7(c) and (d), respectively. The hardness decreased as displacement increased regardless of the strain rates showing the indentation size effect (ISE). ISE was reported previously for many alloys including Cu, Mg and Mg-CNT due to strain gradient plasticity [42–44]. The same behavior was observed for as-build Cu-CNTs which is shown in Fig. 8. As shown in Fig. 8(a) and (b), the Cu-CNTs sample fabricated using LPBF-AM showed lower maximum load under identical displacement, indicating that the hardness of Cu-CNTs composite is lower than the hardness of the Cu sample. Eq. 1 represent the relationship between the hardness and depth as [42]:

$$\frac{H}{H_0} = \sqrt{1 + \frac{h^*}{h}} \tag{1}$$

where, h^* is the length-scale that characterizes ISE of a material while H_o is the depth-independent hardness. According to Eq. (1), the slope and intercept of linear fitting of the H^2 versus $1/h_c$ plot yielded the characteristic length h^* and H_0 of the sample which are presented in Table 1 for AM Cu and Cu-CNTs from top and bottom surfaces at three different strain rates. It can be concluded from Fig. 7(c), (d), Fig. 8(c), and (d) that the ISE is negligible after 1000 nm, therefore the average hardness and reduced modulus for each condition was calculated from 1000 nm to 3000 nm displacement for further analysis and comparison and summarized in Table 1. The hardness and reduced modulus in the range of 1.15–1.5 GPa and 50–85 GPa were observed for LPBF-AM pure Cu. Previous reports showed Vickers hardness in the range of ~ 60–110 HV (~ 0.6–1.1 GPa) for AM Cu with relative density between 82% and 98% [1,36] confirming that the mechanical properties of the parts are seriously affected by the relative density. The same behavior was previously reported for additively manufactured copper–chromium–niobium (Cu-Cr-Nb) alloy, the alloy showed decrease in strength as the porosity increased in thin-wall samples [11]. The Cu sample fabricated using SEBM additive manufacturing technology showed lower hardness of 57.8 HV despite higher relative density of 99.5% which may be due to higher temperature in the SEBM process leading to coarser microstructure [3]. The bulk Cu fabricated using conventional techniques showed hardness of 70–120 HV (~ 0.7–1.2 GPa) [1,45] which is ~ 30% lower than AM Cu in present study. The modulus for conventionally fabricated Cu was 117 GPa [1,45], ~ 60% higher than AM Cu in present study. Cu-CNTs composite showed the hardness and reduced modulus in the range of 0.6–1.1 GPa and 40–80 GPa, respectively (Fig. 8(c) and (d)); ~35% and 10% decrease over hardness and modulus of pure copper, respectively. In similar studies, the hardness of Cu-CNTs composites fabricated using powder metallurgy with 45 µm spherical metal powders (the same powder size as this study) decreased as compared to the copper [46]. However, they showed if Cu particle size was smaller, the hardness increased with addition of CNTs [46]. Further, in [5,47], the metal-CNTs nanocomposites showed greater mechanical properties than pure Cu as a result of nanotube buckling effect. The decrease in mechanical properties of Cu sample with addition of CNTs may be attributed to (i) more porosity in Cu-CNTs sample, (ii) weak interfacial bonding between the CNTs and Cu which may lead to sliding at the interface, (iii) CNT agglomeration, and (iv) degraded CNTs in composites during fabrication process [5,43,48]. This was also reported for other CNT-reinforced materials [49–51].

SRS (denoted by m) is defined according to the power law relation which links hardness (H) to strain rate ($\dot{\varepsilon}$) as follows [38]:

$$H = k\dot{\varepsilon}^m \tag{2}$$

where, k is a material constant. The average hardness from 1000 nm to 3000 nm was calculated (Table 1) and plotted as a function of strain rate for top and bottom surfaces of both as-build Cu and Cu-CNTs in Fig. 9(a) and (b), respectively on double-logarithmic scale.

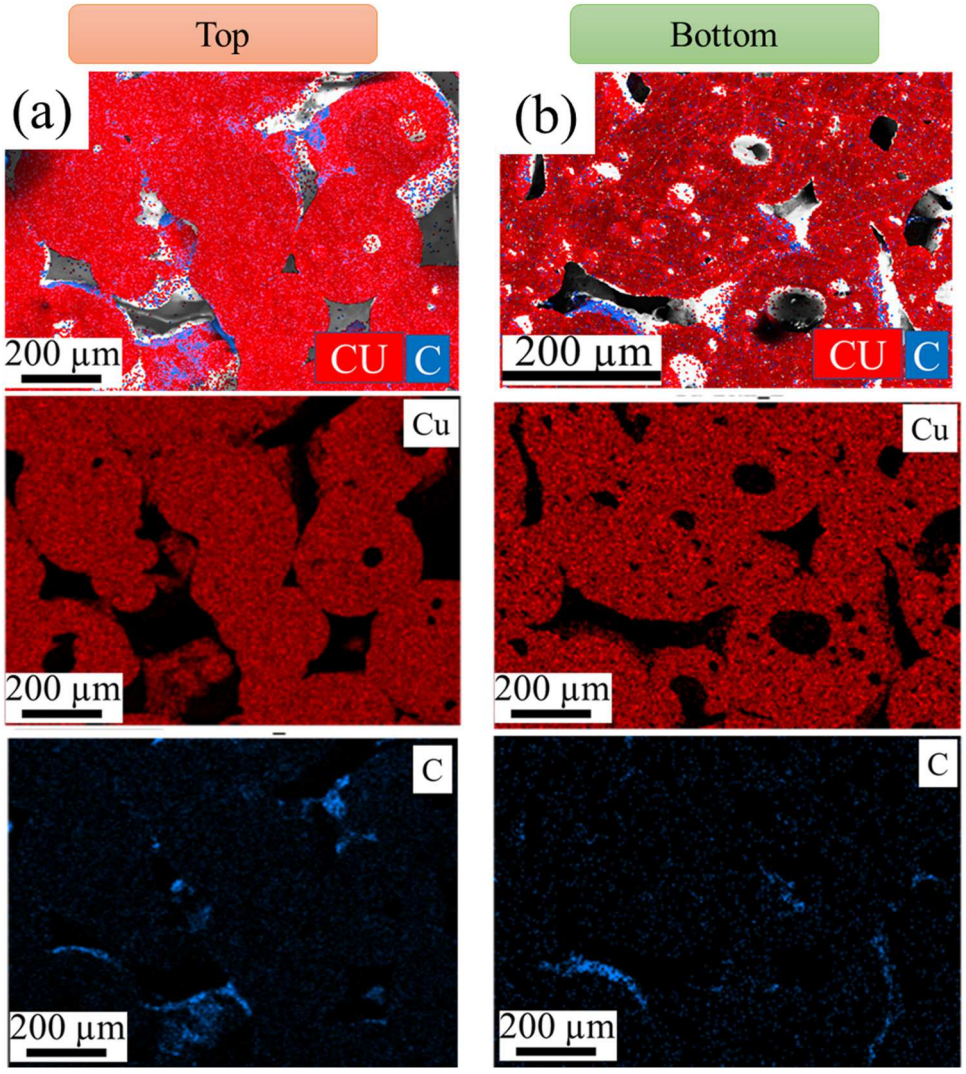

Fig. 6. Energy-dispersive spectroscopy (EDS) mapping of the as-build Cu-CNTs from (a) top surface and (b) bottom surface showing CNTs distribution.

The *m* value is the slope of linear fitting of each curve and indicated alongside the curves in Fig. 9. Top surface of AM fabricated Cu showed slightly lower hardness and ~70% higher SRS as compared to the bottom surface as shown in Fig. 9(a). This might be due to higher porosity on top surface which facilitated easy annihilation of the dislocations or diffusion and thus higher SRS value. For the same reason, Cu-CNTs showed higher SRS (2.8 times for bottom surface and 1.1 times for top surface) than as-build Cu. In addition, Fig. 9(b) shows that both the hardness and SRS was lower for top surface of as-build Cu-CNTs alloy as compared to the bottom surface. The top surface of Cu-CNTs sample showed ~15% lower SRS value as compared to the bottom surface. The same amount of porosity for both surfaces was confirmed from Fig. 5(c) and (d). Therefore, the location-dependent hardness and SRS for as-build Cu-CNTs alloy may be due to other factors rather than porosity such as the grain size. The SRS value in the range of 0.1–0.15 was previously stated for nanocrystalline Cu synthesized using conventional techniques [52]. It has been reported that the strain rate sensitivity of face centered cubic (FCC) metals and alloys increases as grain size decreases [52]. Further, nano-sized twins enhanced the SRS of Cu alloys and Cu-graphite composite [52]. The higher SRS value found in the present study may be due to smaller grain size and cell structure in additively manufactured Cu and Cu-CNTs as well as formation of twinning and higher amount of porosity. Generally, higher SRS values qualitatively indicate good ductility of materials and help to decrease plastic instability [52].

The stress exponent (n) is equal to the reciprocal of strain rate sensitivity (m), and provides valuable insight for identifying deformation mechanisms. Typically, when $n = 1$, the deformation mechanism is associated with diffusion (by lattice or grain boundary diffusion), $n = 2$ with grain boundary sliding, and $n > 3$ with dislocation [53]. According to Fig. 9, the stress exponent was 3.3, 1.5, 1.2, and 1.4 for AM Cu (bottom surface), AM Cu (top surface), AM Cu-CNTs (bottom surface), and AM Cu-CNTs (top surface), respectively. These results indicate dislocation as deformation mechanism for bottom surface of AM Cu and diffusion as the dominated deformation mechanism for other samples. The amount of porosity for Cu-CNTs and Cu (top surface) samples was higher than that for Cu (bottom surface) sample leading to the diffusion as the dominant deformation mechanism.

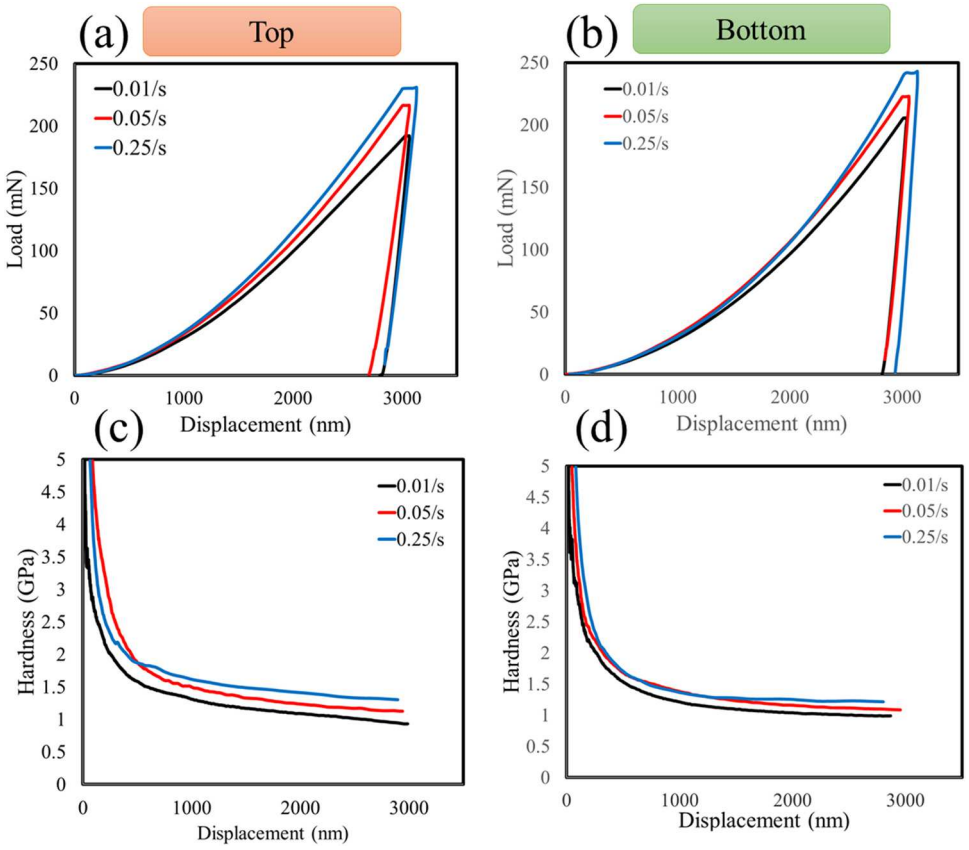

Fig. 7. Representative load-displacement curve as a function of strain rates for AM fabricated Cu from (a) top surface and (b) bottom surface; the corresponding hardness as a function of displacement at three different strain rates for as-build Cu from (c) top surface and (d) bottom surface indicating decrease of hardness as displacement increased.

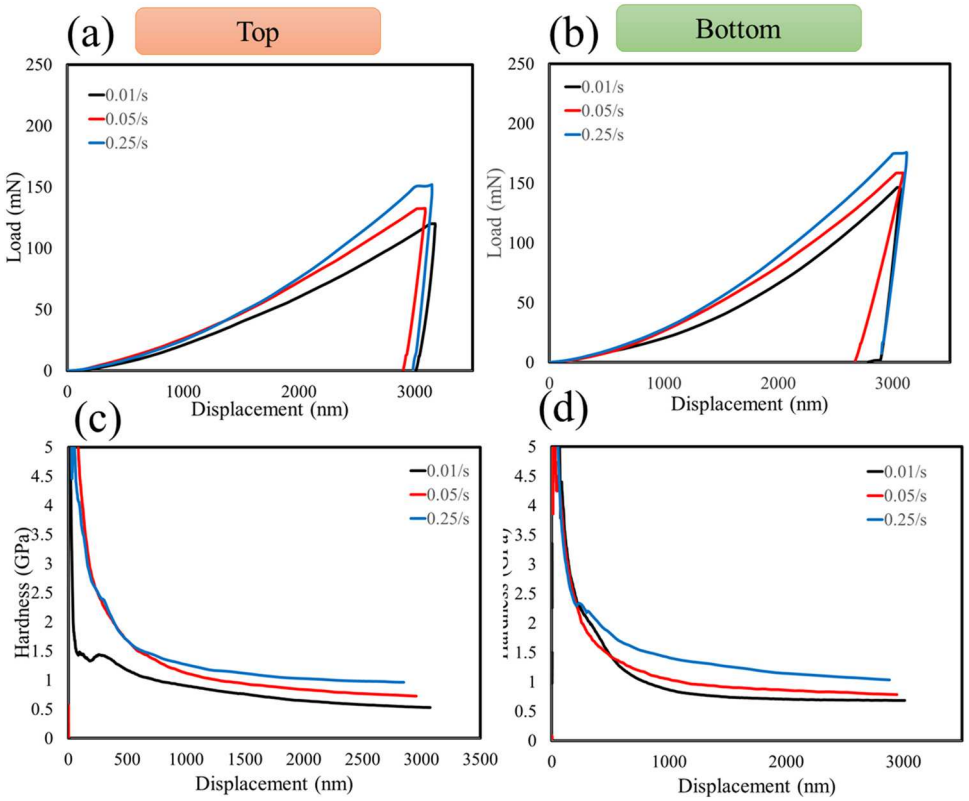

Fig. 8. Representative load-displacement curve at three different strain rates for as-build Cu-CNTs from (a) top surface and (b) bottom surface; the corresponding hardness versus displacement as a function of strain rates for AM fabricated Cu-CNTs from (c) top surface and (d) bottom surface showing decrease of hardness as displacement increased.

Table 1
Summary of length-scale characteristic of indentation size effect (h^*), hardness independent displacement (H_0), average hardness (H_{ave}) and average modulus (E_{ave}) for as-build Cu and Cu-CNTs on top and bottom surfaces at different strain rates.

Alloy	Surfaces	Strain rates (1/s)	h^*(nm)	H_0 (GPa)	H_{ave} (GPa)	E_{ave} (GPa)
Cu	Top	0.01	1300	0.85	1.13	70
		0.05	1450	0.95	1.22	55
		0.25	800	1.2	1.31	50
	Bottom	0.01	1300	0.8	1.4	85
		0.05	1200	0.92	1.43	70
		0.25	760	1.05	1.48	65
Cu-CNTs	Top	0.01	6000	0.3	0.62	65
		0.05	9000	0.35	0.8	60
		0.25	2200	0.7	0.85	40
	Bottom	0.01	2900	0.45	0.8	80
		0.05	2800	0.55	0.92	40
		0.25	1790	0.85	1.1	50

3.3. Creep

In order to evaluate the time-dependent deformation in dwell time, indentation creep test was performed for LPBF-AM Cu and Cu-CNTs. Indentation creep testing is simple, easy to set up, and can be done on any sample size and geometry as small volume of sample is needed [52]. Samples were loaded to predefined displacement of 3000 nm, where ISE is negligible, at a fixed strain rate of 0.05/s and were held for 600 s before unloading. The representative load-displacement plots during creep test for both surfaces of as-build Cu and Cu-CNTs are shown in Fig. 10(a) and (c). The lower hardness for top surface as compared to the bottom surface was observed for both alloys as confirmed from shifting curves to the lower load. Displacement during hold time was used to evaluate the time-dependent deformation behavior, as plotted in Fig. 10(b) and (d) for top and bottom surfaces of as-build Cu and Cu-CNTs, respectively. For AM Cu, the top surface showed ~30% lower creep displacement as compared to the bottom surface, however the opposite trend was observed for as-fabricated Cu-CNTs and top surface showed about three times higher creep displacement than the bottom surface. The amount of creep displacement was consistent with the strain rate sensitivity reported in previous section for each system. Applying force on sample leads to generation of dislocations, some may annihilate from free surfaces or grain boundaries, and some may remain. The lower strain rate sensitivity means lower amount of dislocation are annihilated during loading, therefore more are remained which may be annihilated later while holding, leading to more creep. Overall, the creep displacement was greater for AM Cu-CNTs sample as compared to the as-build Cu. In similar study, the addition of carbon nanotubes to Sn-3.8Ag-0.7Cu (SAC387) solder alloy and Mg led to decrease in creep displacement [43,54]. This was attributed to the interaction of dislocations with nanotubes slowing down their glide and climb [43,54]. The opposite trend observed here may be due to weak interfacial bonding of Cu and CNTs, CNT agglomeration, and degraded CNTs.

Creep displacement (h) as a function of time (t) follows the empirical relation [53]:

$$h(t) = h_0 + a(t - t_0)^p + kt \tag{3}$$

where, a, p and k are fitting constants and h_0 and t_0 are the initial depth and time during creep period. The following relationships are used to obtain indentation strain rate ($\dot{\varepsilon}$)and hardness (H) [53]:

$$\dot{\varepsilon} = \frac{1}{h}\frac{dh}{dt} \tag{4}$$

and

$$H = \frac{P}{24.5\, h_c^2} \tag{5}$$

where, $\frac{dh}{dt}$ is the first derivative of the displacement-time plot with respect to t, P is load, and h_c is contact displacement. The creep strain rate sensitivity was calculated from the slope of $\ln H - \ln\dot{\varepsilon}$ curves and is shown in Fig. 11 (a). Fig. 11 (b) presents the creep stress exponent (n_{creep}, reciprocal of strain rate sensitivity). The average n_{creep} values for all samples were above 3 ($n > 3$), therefore the creep seems to be dominated by dislocation. The degree of stress exponent depends on the balance of dislocations generation and annihilation [53]. Greater stress exponent is obtained when more dislocations are created and involved during deformation. The sharp increase in n value for bottom surface of Cu-CNTs as compared to other samples may be due to enhancement in dislocation generation rather than annihilation.

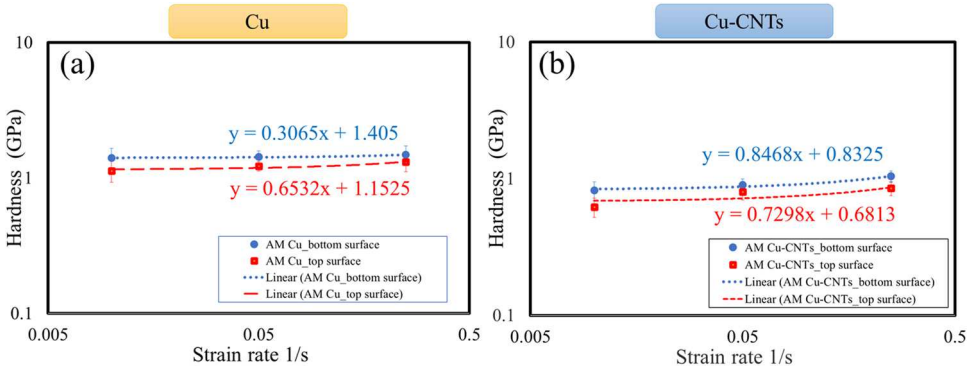

Fig. 9. Log-log plot of hardness versus strain rate for LPBF-AM (a) Cu and (b) Cu-CNTs from both top and bottom surfaces.

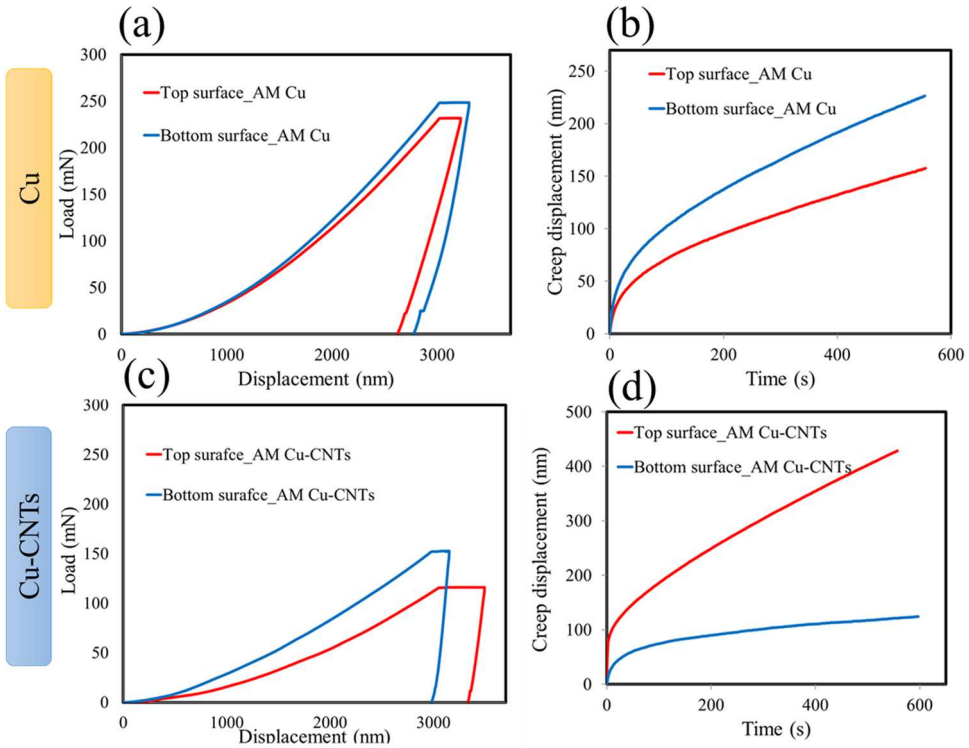

Fig. 10. Nanoindentation creep experiments for LPBF-AM Cu and Cu-CNTs: (a) representative load-displacement for Cu, (b) creep displacement versus holding time for Cu, (c) Load versus displacement plot for Cu-CNTs, and (d) creep displacement as a function of holding time for Cu-CNTs.

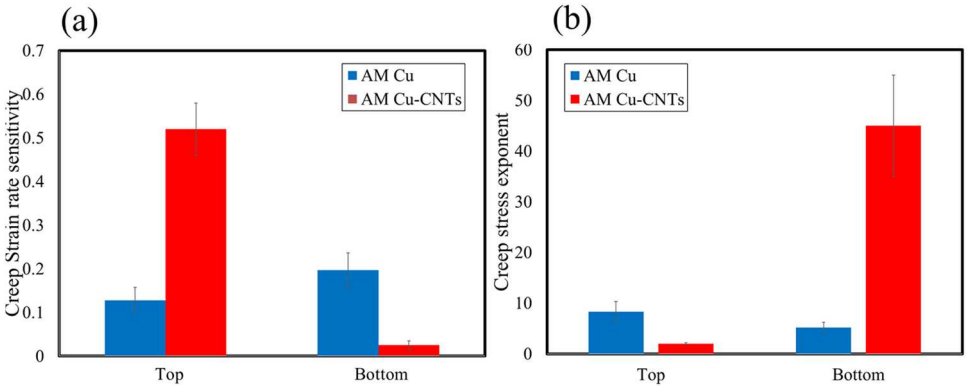

Fig. 11. Creep (a) strain rate sensitivity and (b) stress exponent from top and bottom surfaces of AM Cu and Cu-CNTs samples.

4. Conclusion

In the present study, the strain rate sensitivity and time-dependent plastic deformation (creep) response of copper-carbon nanotube (Cu-CNT) containing 0.5 wt% of CNTs fabricated using laser powder bed fusion additive manufacturing (LPBF-AM) was investigated through instrumented nanoindentation tests at room temperature in comparison to as-build pure Cu. The effect of distance from build plat on microstructure and nanomechanical properties of both samples were also evaluated. The results showed that the addition of CNTs led to increase in porosity of sample and consequently decrease in hardness, increase in strain rate sensitivity (SRS) and creep displacement as compared to the pure Cu fabricated at the identical condition. The hardness decrease and creep displacement increase may also be due to weak interfacial bonding of Cu and CNTs, CNT agglomeration, and degraded CNTs. Further, location-dependent properties were observed for both samples with the top surface showing lower hardness than the bottom surface for both as-build Cu and Cu-CNTs. Although the strain rate sensitivity value was greater for top surface of as-build Cu as compared to the bottom surface due to the effect of porosity, the top surface of as-fabricated Cu-CNTs showed lower SRS than the bottom probably due to the effect of grain size. The dislocation was the dominant deformation mechanism for bottom surface of AM Cu and for other samples, the diffusion was the main deformation mechanism. However, the creep mechanism was dominated by dislocation for all samples. These materials are promising candidates as conductor in many applications including aerospace, automotive, and electric fields. The findings of this work may be used for material selection in these industries. This study may also be used as a reference for fundamental understanding of location-, strain rate-, and time-dependent deformation mechanism on other nanocomposites.

CRediT authorship contribution statement

Leila Ladani: Idea generation, Experiment outline, Methodology, Experimental procedures, **Maryam Sadeghilaridjani:** Experiment implementation, First draft.

Declaration of Competing Interest

The authors declare that they have no known competing financial interests or personal relationships that could have appeared to influence the work reported in this paper.

Acknowledgement

The authors acknowledge the Eyring Materials Center at ASU for access to advanced characterization techniques. The authors would also like to acknowledge the Innovation Hub in Polytechnic School campus, ASU for additive manufacturing of the samples.

References

[1] L. Constantin, Z. Wu, N. Li, L. Fan, J.F. Silvain, Y.F. Lu, Laser 3D printing of complex copper structures, Addit. Manuf. 35 (2020), https://doi.org/10.1016/j.addma.2020.101268
[2] M.A. Lodes, R. Guschlbauer, C. Körner, Process development for the manufacturing of 99.94% pure copper via selective electron beam melting, Mater. Lett. 143 (2015) 298–301, https://doi.org/10.1016/j.matlet.2014.12.105
[3] Q. Jiang, et al., A review on additive manufacturing of pure copper, Coatings 11 (6) (2021), https://doi.org/10.3390/coatings11060740
[4] R.M. Sundaram, A. Sekiguchi, M. Sekiya, T. Yamada, K. Hata, Copper/Carbon Nanotube Composites: Research Trends and Outlook, Royal Society Open Science, 5 Royal Society Publishing, 2018, https://doi.org/10.1098/rsos.180814
[5] G. Chai, Y. Sun, J. Sun, Q. Chen, Mechanical properties of carbon nanotube-copper nanocomposites, J. Micromech. Microeng. 18 (3) (2008), https://doi.org/10.1088/0960-1317/18/3/035013
[6] L. Ladani, Multi-scale Manufacturing of Carbon Nanotube Composites, no. 1658254.109US0. pp. 1–19, 2016.
[7] I. Awad, L. Ladani, Cohesive zone model for the interface of multiwalled carbon nanotubes and copper: molecular dynamics simulation, J. Nanotechnol. Eng. Med. 5 (3) (2014) 1–7, https://doi.org/10.1115/1.4029462
[8] I. Awad, L. Ladani, Interfacial strength between single wall carbon nanotubes and copper material: molecular dynamics simulation, J. Nanotechnol. Eng. Med. 4 (4) (2014), https://doi.org/10.1115/1.4026939
[9] I. Awad, L. Ladani, Mechanical integrity of a carbon nanotube/copper-based through-silicon via for 3D integrated circuits: a multi-scale modeling approach, Nanotechnology 26 (48) (2015), https://doi.org/10.1088/0957-4484/26/48/485705
[10] L. Ladani, I. Awad, Y. She, S. Dardona, W. Schmidt, Fabrication of carbon nanotube/copper and carbon nanofiber/copper composites for microelectronics, Mater. Today Commun. 11 (2017) 123–131, https://doi.org/10.1016/j.mtcomm.2017.03.004
[11] G. Demeneghi, B. Barnes, P. Gradl, J.R. Mayeur, K. Hazeli, Size effects on microstructure and mechanical properties of additively manufactured copper–chromium–niobium alloy, Mater. Sci. Eng. A 820 (2021) 141511, https://doi.org/10.1016/j.msea.2021.141511
[12] A. Popovich, V. Sufiiarov, I. Polozov, E. Borisov, D. Masaylo, A. Orlov, Microstructure and mechanical properties of additive manufactured copper alloy, Mater. Lett. 179 (2016) 38–41, https://doi.org/10.1016/j.matlet.2016.05.064
[13] L. Ladani, M. Sadeghilaridjani, Review of powder bed fusion additive manufacturing for metals, Metals 11 (9) (2021), https://doi.org/10.3390/met11091391
[14] L. Ladani, Local and global mechanical behavior and microstructure of Ti6Al4V parts built using electron beam melting technology, Metall. Mater. Trans. A: Phys. Metall. Mater. Sci. 46 (9) (2015) 3835–3841, https://doi.org/10.1007/s11661-015-2965-6
[15] L. Ladani, Additive Manufacturing of Metals: Materials, Processes, Tests, and Standards. DEStech Publications, Incorporated, 2020.
[16] L. Awad,Ibrahim; Ladani, "No Title," Proceedings of the ASME 2014 International Mechanical Engineering Congress and Exposition IMECE2014 November 14–20, 2014, Montreal, Quebec, Canada, 2014.
[17] F. Ahsan, L. Ladani, Temperature profile, bead geometry, and elemental evaporation in laser powder bed fusion additive manufacturing process, Jom 72 (1) (2020) 429–439, https://doi.org/10.1007/s11837-019-03872-3
[18] R. Andreotta, L. Ladani, W. Brindley, Finite element simulation of laser additive melting and solidification of Inconel 718 with experimentally tested thermal properties, Finite Elem. Anal. Des. 135 (2017) 36–43, https://doi.org/10.1016/j.finel.2017.07.002
[19] F. Ahsan, J. Razmi, L. Ladani, Multi-physics modeling of laser interaction with surface in powder bed melting process, ASME International Mechanical Engineering Congress and Exposition, Proceedings (IMECE), 2, no. November, 2018, doi: 10.1115/IMECE2018–86566.
[20] J. Romano, L. Ladani, M. Sadowski, Laser additive melting and solidification of inconel 718: finite element simulation and experiment, Jom 68 (3) (2016) 967–977, https://doi.org/10.1007/s11837-015-1765-1
[21] J. Romano, L. Ladani, M. Sadowski, Thermal modeling of laser based additive manufacturing processes within common materials, Procedia Manuf. 1 (2015) 238–250, https://doi.org/10.1016/j.promfg.2015.09.012
[22] A. Keshavarzkermani, M. Sadowski, L. Ladani, Direct metal laser melting of Inconel 718: process impact on grain formation and orientation, J. Alloy. Compd. 736 (2018) 297–305, https://doi.org/10.1016/j.jallcom.2017.11.130
[23] M.J. Mian, J. Razmi, L. Ladani, Mechanical behavior of electron beam powder bed fusion additively manufactured Ti6Al4V parts at elevated temperatures, J. Manuf. Sci. Eng., Trans. ASME 143 (2) (2021) 1–12, https://doi.org/10.1115/1.4049092
[24] L. Ladani, J. Razmi, S.F. Choudhury, Mechanical anisotropy and strain rate dependency behavior of Ti6Al4V produced using E-beam additive fabrication, J. Eng. Mater. Technol., Trans. ASME 136 (3) (2014) 1–7 10.1115/1.4027729.
[25] L. Ladani, J. Romano, W. Brindley, S. Burlatsky, Effective liquid conductivity for improved simulation of thermal transport in laser beam melting powder bed technology, Addit. Manuf. 14 (2017) 13–23, https://doi.org/10.1016/j.addma.2016.12.004
[26] M. Sadowski, L. Ladani, W. Brindley, J. Romano, Optimizing quality of additively manufactured Inconel 718 using powder bed laser melting process, Addit. Manuf. 11 (2016) 60–70, https://doi.org/10.1016/j.addma.2016.03.006
[27] J. Romano, L. Ladani, J. Razmi, M. Sadowski, Temperature distribution and melt geometry in laser and electron-beam melting processes - a comparison among common materials, Addit. Manuf. 8 (2015) 1–11, https://doi.org/10.1016/j.addma.2015.07.003
[28] S.A. Shanmugasundaram, J. Razmi, M.J. Mian, L. Ladani, Mechanical anisotropy and surface roughness in additively manufactured parts fabricated by stereolithography (SLA) using statistical analysis, Materials 13 (11) (2020), https://doi.org/10.3390/ma13112496
[29] R. Lehnert, et al., Microstructural and mechanical characterization of high-alloy quenching and partitioning TRIP steel manufactured by electron beam melting, Mater. Sci. Eng. A 794 (2020), https://doi.org/10.1016/j.msea.2020.139684
[30] J. Shittu, et al., Tribo-corrosion response of additively manufactured high-entropy alloy, npj Mater. Degrad. 5 (1) (2021) 1–8, https://doi.org/10.1038/s41529-021-00177-2
[31] H.H. Zhu, L. Lu, J.Y.H. Fuh, Development and characterisation of direct laser sintering Cu-based metal powder, J. Mater. Process. Technol. 140 (1–3) (2003) 314–317, https://doi.org/10.1016/S0924-0136(03)00755-6
[32] D. Gu, Y. Shen, S. Fang, J. Xiao, Metallurgical mechanisms in direct laser sintering of Cu-CuSn-CuP mixed powder, J. Alloy. Compd. 438 (1–2) (2007) 184–189, https://doi.org/10.1016/j.jallcom.2006.08.040
[33] Y. Tang, H.T. Loh, Y.S. Wong, J.Y.H. Fuh, L. Lu, X. Wang, Direct laser sintering of a copper-based alloy for creating three-dimensional metal parts, J. Mater. Process. Technol. 140 (1–3) (2003) 368–372, https://doi.org/10.1016/S0924-0136(03)00766-0
[34] S.D. Jadhav, S. Dadbakhsh, L. Goossens, J.P. Kruth, J. van Humbeeck, K. Vanmeensel, Influence of selective laser melting process parameters on texture evolution in pure copper, J. Mater. Process. Technol. 270 (2019) 47–58, https://doi.org/10.1016/j.jmatprotec.2019.02.022
[35] C. Silbernagel, L. Gargalis, I. Ashcroft, R. Hague, M. Galea, P. Dickens, Electrical resistivity of pure copper processed by medium-powered laser powder bed fusion additive manufacturing for use in electromagnetic applications, Additive Manuf. 29 (2019), https://doi.org/10.1016/j.addma.2019.100831
[36] S.D. Jadhav, J. Vleugels, J.P. Kruth, J. van Humbeeck, K. Vanmeensel, Mechanical and electrical properties of selective laser-melted parts produced from surface-oxidized copper powder, Mater. Des. Process. Commun. 2 (2) (2020), https://doi.org/10.1002/mdp2.94
[37] J. Liu, et al., Mechanical properties and failure mechanisms at high temperature in carbon nanotube reinforced copper matrix nanolaminated composite, Compos. Part A: Appl. Sci. Manuf. 116 (2019) 54–61, https://doi.org/10.1016/j.compositesa.2018.10.022
[38] M. Sadeghilaridjani, S. Muskeri, V. Hassannaeimi, M. Pole, S. Mukherjee, Strain rate sensitivity of a novel refractory high entropy alloy: Intrinsic versus extrinsic effects, Mater. Sci. Eng. A 766 (2019) 138326, https://doi.org/10.1016/j.msea.2019.138326
[39] S. Muskeri, V. Hasannaeimi, R. Salloom, M. Sadeghilaridjani, S. Mukherjee, Small-scale mechanical behavior of a eutectic high entropy alloy, Sci. Rep. 10 (1) (2020) 1–12, https://doi.org/10.1038/s41598-020-59513-2
[40] M. Sadeghilaridjani, M. Pole, S. Jha, S. Muskeri, N. Ghodki, S. Mukherjee, Deformation and tribological behavior of ductile refractory high-entropy alloys, Wear 478–479 (2021), https://doi.org/10.1016/j.wear.2021.203916
[41] M. Dao, L. Lu, Y.F. Shen, S. Suresh, Strength, strain-rate sensitivity and ductility of copper with nanoscale twins, Acta Mater. 54 (20) (2006) 5421–5432, https://doi.org/10.1016/j.actamat.2006.06.062
[42] M. Sadeghilaridjani, S. Mukherjee, Strain gradient plasticity in multiprincipal element alloys, Jom 71 (10) (2019) 3466–3472, https://doi.org/10.1007/s11837-019-03703-5
[43] J. Thornby, et al., Micromechanics and indentation creep of magnesium carbon nanotube nanocomposites: 298 K–573 K, Mater. Sci. Eng. A 801 (2021), https://doi.org/10.1016/j.msea.2020.140418
[44] W.D. Nix*$, H. Gao, Indentation Size Effects in Crystalline Materials: A Law for Strain Gradient Plasticity, 1998.
[45] M. Li, S.J. Zinkle, 4.20 Physical and Mechanical Properties of Copper and Copper Alloys.

[46] S.M. Uddin, et al., Effect of size and shape of metal particles to improve hardness and electrical properties of carbon nanotube reinforced copper and copper alloy composites, Compos. Sci. Technol. 70 (16) (2010) 2253–2257, https://doi.org/10.1016/j.compscitech.2010.07.012
[47] W.X. Chen, J.P. Tu, L.Y. Wang, H.Y. Gan, Z.D. Zu, X.B. Zhang, Tribological application of carbon nanotubes in a metal-based composite coating and composites, Carbon 41 (2) (2003) 215–222.
[48] Z. Hu, et al., Laser additive manufacturing bulk graphene-copper nanocomposites, Nanotechnology 28 (44) (2017), https://doi.org/10.1088/1361-6528/aa8946
[49] X. Wang, N.P. Padture, H. Tanaka, Contact-damage-resistant ceramic/single-wall carbon nanotubes and ceramic/graphite composites, Nat. Mater. 3 (8) (2004) 539–544, https://doi.org/10.1038/nmat1161
[50] C.L. Xu, B.Q. Wei, R.Z. Ma, J. Liang, X.K. Ma, D.H. Wu, Fabrication of aluminum-carbon nanotube composites and their electrical properties, 1999.
[51] G.D. Zhan, J.D. Kuntz, J. Wan, A.K. Mukherjee, Single-wall carbon nanotubes as attractive toughening agents in alumina-based nanocomposites, Nat. Mater. 2 (1) (2003) 38–42, https://doi.org/10.1038/nmat793
[52] M. Cabibbo, C. Paoletti, B. Lasio, R. Orrù, F. Delogu, Indentation strain rate sensitivity of ball-milled spark-plasma sintered Cu-C metal matrix composite, J. Alloy. Compd. 767 (2018) 838–847, https://doi.org/10.1016/j.jallcom.2018.07.155
[53] M. Sadeghilaridjani, S. Mukherjee, High-temperature nano-indentation creep behavior of multi-principal element alloys under static and dynamic loads, Metals 10 (2) (2020), https://doi.org/10.3390/met10020250
[54] V.L. Niranjani, V. Singh, B.S.S. Chandra Rao, S. v Kamat, Creep behaviour of SAC387 lead free solder alloy reinforced with single walled carbon nanotubes, Trans. Indian Inst. Met. 68 (2) (2015) 311–317 10.1007/s12666-014-0458-8.